

Research Paper

Eulerian-Lagrangian model for simulation of flow behavior and heat transfer of lab scale dual circulating fluidized beds[☆]

Junchao Yang^a, Dongkuan Zhang^a, Li Liu^b, Yuanbo Xie^c, Yingnan Du^c, Aimin Li^a, Changlei Qin^{d,*}, Guozhao Ji^{a,*}

^a Key Laboratory of Industrial Ecology and Environmental Engineering of Ministry of Education, School of Environmental Science and Technology, Dalian University of Technology, Dalian 116000, PR China

^b Anhui Conch Biomass Energy Technol Co Ltd, Wuhu 241000 Anhui, PR China

^c Tianyun Low-carbon New Energy Technology Co Ltd, Dalian 116033, PR China

^d Key Laboratory of Low-grade Energy Utilization Technologies and Systems of Ministry of Education, School of Energy and Power Engineering, Chongqing University, Chongqing 400044, PR China

ARTICLE INFO

Keywords:

Fluidized bed
Computational fluid dynamics
Lagrangian particles
Gas solid flow
Barracuda

ABSTRACT

Eulerian-Lagrangian model played an important role in simulating and interpreting the multiphase flow behavior in fluidized beds. This study investigated the gas-solid fluid dynamics and heat transfer in a three-dimensional lab-scale circulating fluidized bed (CFB) for the calcium looping process using the multiphase-particle-in-cell (MP-PIC) method. Analyses were conducted on particle residence time distribution (RTD) and solid back-mixing behavior under both thermal and cold conditions. The results indicated that the carbonator exhibited a standard “core-annulus structure” in axial velocity and particle distribution under stable conditions, while the regenerator demonstrated an irregular distribution pattern due to gas-solid exchanges with downstream components and inter-particle collisions within the reactor, indicating heterogeneity in flow behavior, which might affect the product homogeneity in future applications. Thermal-state simulations revealed that excessive gas flow velocities led to significant particle accumulation at the regenerator outlet and reverse flow to the upstream loop seal, highlighting the incompatibility of cold-state parameters for thermal-state operation. Moreover, both reactors showcased uneven distributions of particle residence time, with certain particles exhibiting extended residence times, characterized by the presence of an “early peak and long tail” in the RTD profile. A pronounced back-mixing phenomenon was identified, particularly in the regenerator, where the degree of mixing diminished with height. Particle velocity analysis revealed downward movements in the bottom regions, contributing to prolonged residence times. The temperature distribution in the CFB showed that the particles in the regenerator could reach the desired temperature, but the particles in the carbonator were 100–200 K lower than the set temperature of the reactor wall due to the insufficient residence time. These insights provide critical understanding for optimizing the design and operation of CFB systems for calcium looping applications.

1. Introduction

The significant increase in atmospheric CO₂ levels is the primary cause of global warming. The World Meteorological Organization reported that the average volume fraction of global atmospheric CO₂ has risen from 2.80×10^{-4} before the Industrial Revolution to 4.21×10^{-4} in 2023. In 2021, the global average temperature was (1.11 ± 0.13) degrees higher than that before industrialization, causing significant risk

to the global environment and human life [1,2]. In 2016, over 170 countries signed the Paris Agreement, which aims to limit the global temperature increase to below 2 °C, and to strive to keep it within 1.5 °C [3]. To achieve this goal, global carbon emissions must be reduced to below 49 % of 2017 levels by 2030 [4]. To this end, the European Union, the United Kingdom, and Canada have planned to achieve carbon neutrality by 2050. The Chinese government has committed to striving to reach a ‘carbon peak’ before 2030 and achieve ‘carbon neutrality’

* This article is part of a special issue entitled: ‘CFB-14’ published in Applied Thermal Engineering.

* Corresponding authors.

E-mail addresses: c.qin@cqu.edu.cn (C. Qin), guozhaoji@dlut.edu.cn (G. Ji).

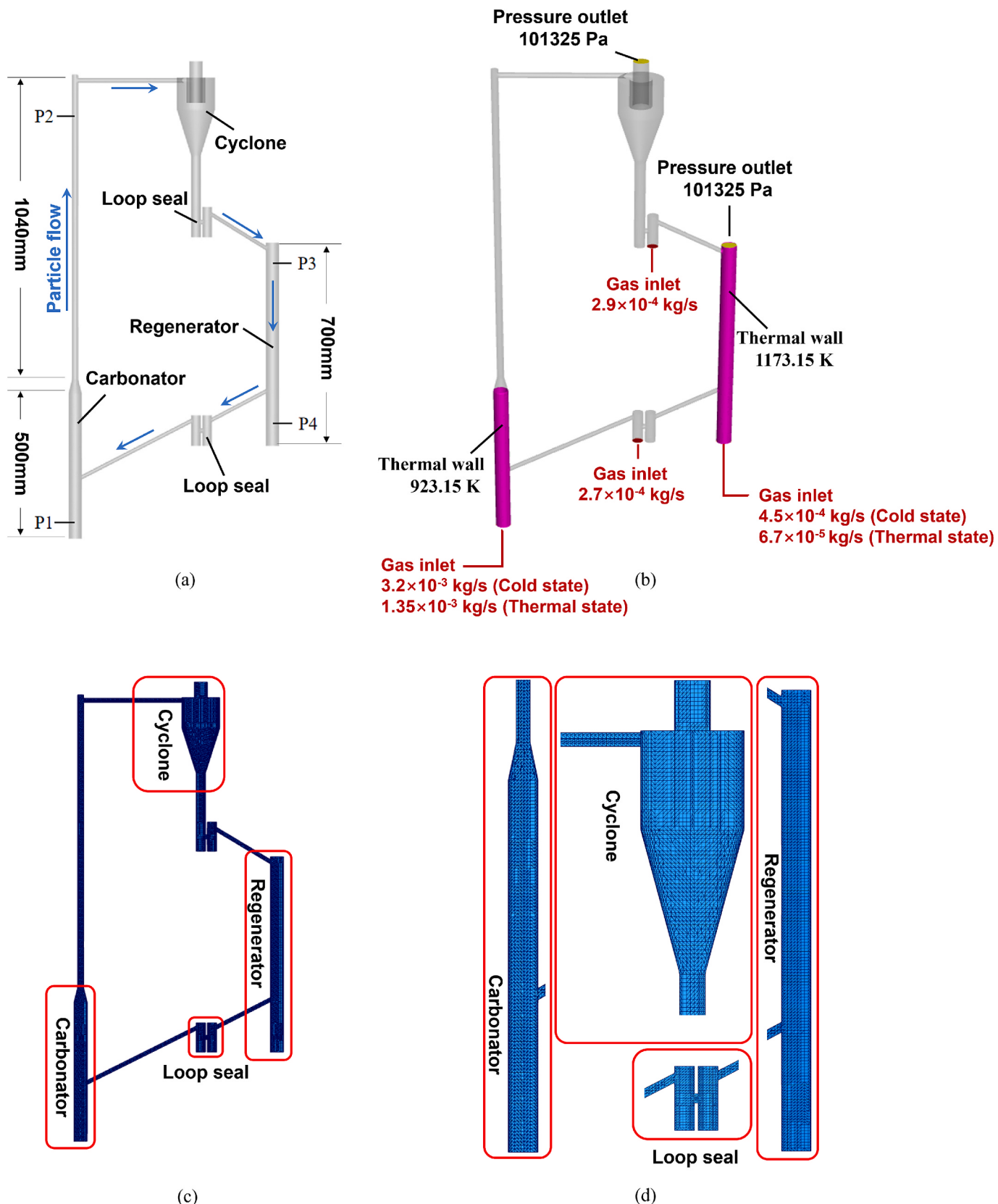


Fig. 1. Lab scale circulating fluidized bed. (a) Geometry configuration; (b) Boundary condition settings; (c) Computational grids; (d) Enlarged view of the grids in key parts.

Table 1
Simulation parameters used in fluidized bed model.

Parameters	Carbonator	Regenerator	ULS	LLS
Reactor diameter (m)	0.042	0.042	0.03	0.03
Reactor height (m)	0.5	0.7	—	—
Inlet gas temperature (K)	300	300	300	300
Initial bed temperature in the cold state (K)	300	300	—	—
Initial bed temperature in the thermal state (K)	923.15	1173.15		
Inlet mass flow rate in the cold state (kg/s)	3.2×10^{-3}	4.5×10^{-4}	2.9×10^{-4}	2.7×10^{-4}
Inlet mass flow rate in the thermal state (kg/s)	1.35×10^{-3}	6.7×10^{-5}	2.9×10^{-4}	2.7×10^{-4}
Initial particle accumulation height (m)		0.27		
Solid volume fraction at close pack (—)	0.6			
particle normal-to-wall retention coefficient (—)	0.1			
particle tangential-to-wall retention coefficient (—)	0.99			
Time step (s)	1×10^{-4}			
Outlet pressure (Pa)	101,325			

before 2060 [5]. While waiting for renewable energy technologies to fully mature and replace fossil fuels, it is also crucial to address the carbon emissions from fossil energy through Carbon Capture, Utilization, and Storage (CCUS) technologies [6].

The capture of CO₂ is typically the most critical and the most expensive part of CCUS projects, generally accounting for 60 % to 70 % of the total costs [7]. In these projects, CO₂ is usually captured from a large and fixed source of CO₂ emissions, followed by steps of separation, collection, and compression, enabling subsequent transportation, utilization, and storage [8,9]. The CO₂ emitted by energy power plants and high-emission industries such as steel and cement accounts for 70 % of global CO₂ emissions. As these emissions are dense and fixed, they represent one of the most suitable carbon sources. Capturing CO₂ at these sites is efficient in terms of investment cost and emission reduction.

CaO (calcium oxide) is considered an ideal high-temperature capture material due to its low cost, abundant calcium sources, high theoretical adsorption capacity (78.6 wt%), and fast adsorption/desorption kinetics (0.1–0.4 g·CO₂ g⁻¹ min⁻¹) [10–12]. Its effective adsorption temperature can reach up to 850 °C, which is higher than that of most other solid adsorbents, thus favoring the sorption rate. The average cost of capturing carbon dioxide is estimated to be between \$29 and \$50 per ton of CO₂, which is over 50 % lower than that of amine scrubbing [13]. Under high temperatures, CaO is carbonated to form CaCO₃, which then reverts to CaO after thermal decarbonization. The exothermic carbonation reaction of CaO with CO₂ and the endothermic calcination reaction are illustrated in Eqs. (1) and (2), forming a cyclic process [14,15].



The concept of calcium looping (CaL) capturing CO₂ from a power plant has been proposed long before. In calcium looping, CO₂ from the flue gas at the tail end of a power plant is absorbed by CaO in the

carbonator at temperatures of about 650–700 °C, forming CaCO₃. The heat generated from this exothermic reaction could be utilized for power generation. The generated CaCO₃ is then transferred to the regenerator, where it completely decomposes back to CaO at high temperatures of 900–950 °C [16], produced by the oxy-fuel combustion of coal and other fuels. The resulting CaO is then sent back to the carbonator to absorb CO₂ again, allowing for repeated sorption/desorption cycles. However, the calcium looping concept was only demonstrated in fixed-bed reactors. Instead of transporting CaO or CaCO₃ between two fluidized bed reactors, existing research studies switch reactor temperatures between 650–700 °C and 900–950 °C to represent the carbonation sorption and decarbonation regeneration. For example, Coppola et al. investigated the CO₂ capture capacity of six limestones during calcium looping under alternating calcification-carbonation conditions [17]. Gao et al. performed gasification of sawdust in a CO₂ atmosphere with CaO in a temperature-switching fixed-bed reactor [18]. Even though this configuration demonstrated the feasibility of calcium looping, the effect or performance might be very different from the calcium sorbent application in real scenarios, due to the difference in residence time, thermal history, reaction kinetics, etc.

The main obstacle in the circulating-fluidized-bed test for calcium looping is the difficulty in controlling the flow and particles. The traditional approach for a fluidized-bed trial run is to build a transparent glass fluidized bed with identical geometries, and run gas–solid flow in cold mode. Thanks to the transparency of the glass, the two-phase flow details could be visualized and monitored. However, in the thermal mode test, due to the opaqueness of the furnace and steel reactor wall, it is impossible to visualize the details in the reactor by experimental measurements. Computer simulation is a practical approach to obtaining information inside reactors [19–21]. The Eulerian-Lagrangian method is able to capture the gas–solid flow behavior. Eulerian-Lagrangian method is generally categorized into computational fluid dynamics combined with discrete element methods (CFD-DEM) and multiphase particle-in-cell methods (MP-PIC). Specifically, CFD-DEM can track the trajectory of each real particle [22–24]. However, when modeling large-scale reactors with millions or billions of particles, CFD-DEM cannot withstand the enormous amount of computation [25]. The MP-PIC method combines the advantages of the Eulerian-Eulerian and CFD-DEM methods by grouping multiple real particles with the same properties (position, temperature, particle size, etc.) into a single numerical parcel, and introduces a stress model for the particle collision process so that the number of computed particles in the simulation is reduced significantly [12]. Previous studies have shown that most fluidized bed simulations analyze the gas–solid flow behavior inside the fluidized bed in cold or thermal states. This study analyzed the particle flow characteristics inside the fluidized bed in the cold and thermal states, respectively. The details of gas–solid flow for Ca-looping CO₂ capture, such as velocity distribution, solid concentration, and particle thermal history, could be obtained in this work. Additionally, the residence time of particles in the reactor is analyzed in conjunction with heat transfer. This study could provide practical reference or guidance for the next-generation research on calcium looping.

2. Modeling details

In this study, Barracuda Virtual Reactor 24.0.0 was used to solve the gas–solid flow in three dimensions. The detailed governing equations and drag model are shown below.

2.1. Governing equations

The model needs to simulate both the gas phase flow and particle flow. The gas phase as a continuum is solved for the motion of the fluid using the averaged Navier-Stokes equations. The continuity and momentum conservation equations are as follows [26,27]:

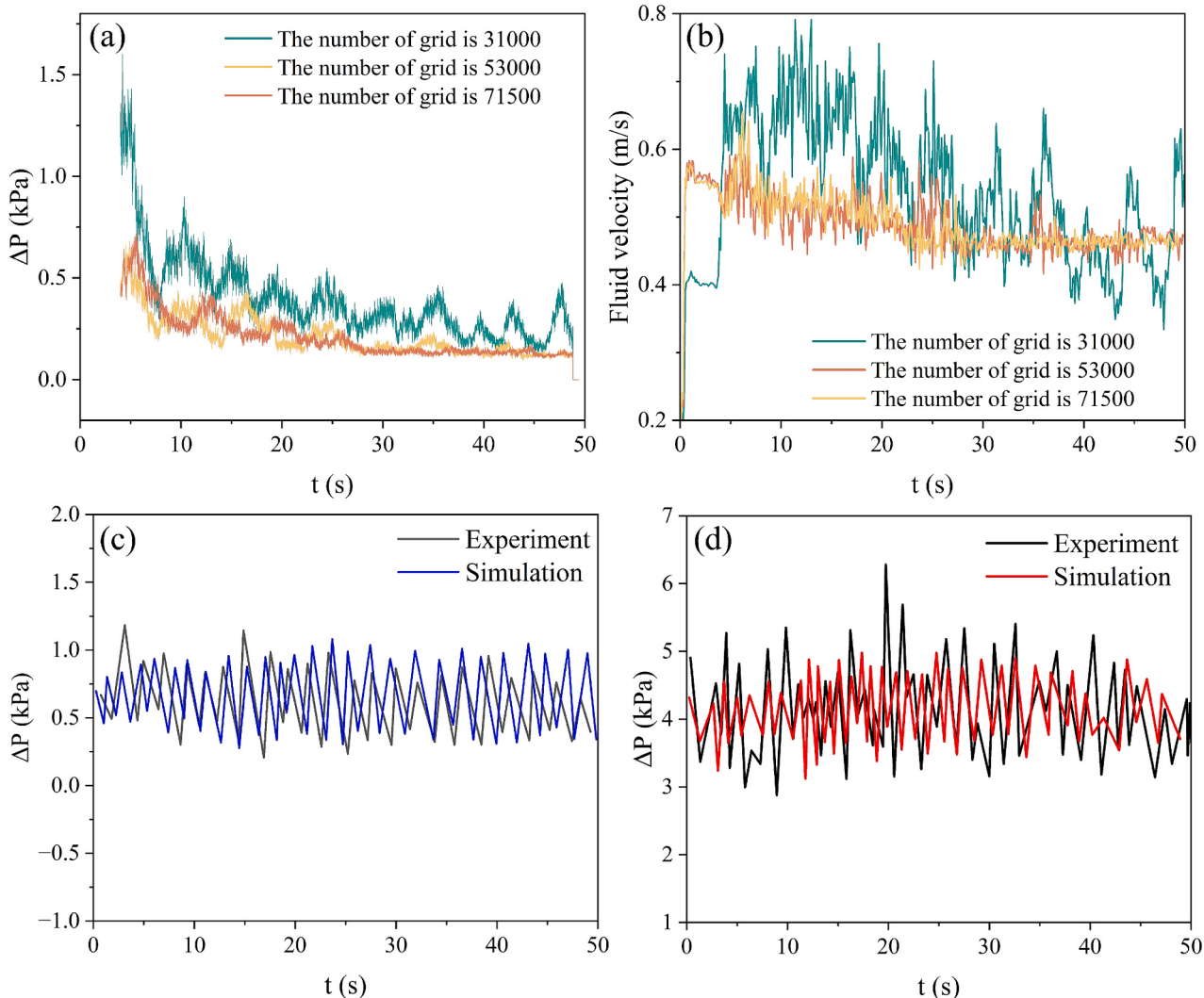


Fig. 2. Mesh independence analysis and model validation. (a) Pressure drop evolution in carbonator with different meshes; (b) Evolution of fluid velocity at the cyclone outlet with different meshes; (c) Comparison of simulation pressure drop with experimental pressure drop in the carbonator; (d) Comparison of simulation pressure drop with experimental pressure drop in the regenerator.

$$\frac{\partial(\varepsilon_g \rho_g)}{\partial t} + \nabla \cdot (\varepsilon_g \rho_g \mathbf{u}_g) = 0 \quad (3)$$

$$\frac{\partial(\varepsilon_g \rho_g \mathbf{u}_g)}{\partial t} + \nabla \cdot (\varepsilon_g \rho_g \mathbf{u}_g \mathbf{u}_g) = -\varepsilon_g \nabla p + \nabla \cdot (\varepsilon_g \tau_g) + \varepsilon_g \rho_g \mathbf{g} - \mathbf{F}_{gs} \quad (4)$$

where \mathbf{u}_g represents the velocity of gas, $\text{m} \cdot \text{s}^{-1}$. p is the pressure of gas, Pa . ρ_g is the density of the gas phase, $\text{kg} \cdot \text{m}^{-3}$. ε_g denotes the gas volume fraction. \mathbf{g} is the gravitational acceleration, $\text{m} \cdot \text{s}^{-2}$. \mathbf{F}_{gs} is the source term caused by the momentum exchange between the gas-phase and solid phase, $\text{N} \cdot \text{m}^{-3}$ [27]. τ_g is the macroscopic gas stress, $\text{N} \cdot \text{m}^{-2}$.

$$\mathbf{F}_{gs} = \iiint f_s V_s \rho_s \left[D_s (\mathbf{u}_g - \mathbf{u}_s) - \frac{1}{\rho_s} \nabla p \right] dV_s d\rho_s du_s \quad (5)$$

where f_s is the probability distribution function of solid particles, $\text{s}^3 \cdot \text{m}^{-6}$. V_s is the volume of the solid particles, m^3 . ρ_p is particle density, $\text{kg} \cdot \text{m}^{-3}$. \mathbf{u}_s is particle velocity vector of the solid particles, $\text{m} \cdot \text{s}^{-1}$. D_s refers to the drag function at the particle location, s^{-1} .

Particle interactions are modeled through the use of a computationally efficient particle stress function. The stress function is [28]:

$$\varphi(\theta_p) = \frac{10P_s \theta_p^\beta}{\max[\theta_{cp} - \theta_p, \lambda(1 - \theta_p)]} \quad (6)$$

where P_s is a constant with units of pressure, Pa . θ_{cp} is the particle volume fraction at close pack. θ_p is the particle volume fraction. β is a constant with a recommended value between 2 and 5. λ is a very small number [29].

Heat transfer between the fluid phase and the particle phase is modeled by the fluid-to-particle heat transfer coefficient. The general form of the fluid-to-particle heat transfer coefficient is [30,31].

$$h_p = \left(c_0 Re_p^{n_1} Pr^{0.33} + c_1 \right) \frac{k_g}{d_p} + c_2 \quad (7)$$

where c_0 , c_1 , c_2 , and n_1 are adjustable model parameters. k_g is the thermal conductivity of the gas, $\text{W} \cdot \text{m}^{-1} \cdot \text{K}^{-1}$. d_p is the particle diameter, m . The Reynolds number and Prandtl number are defined as [30,31]:

$$Re = \frac{\rho_g |\mathbf{u}_g - \mathbf{u}_p| d_p}{\mu_g} \quad Pr = \frac{\mu_g c_{p,g}}{k_f} \quad (8)$$

where \mathbf{u}_p is the particle velocity, $\text{m} \cdot \text{s}^{-1}$. μ_g is the fluid viscosity, $\text{kg} \cdot \text{m}^{-1} \cdot \text{s}^{-1}$. $c_{p,g}$ is the fluid heat capacity, $\text{J} \cdot \text{kg}^{-1} \cdot \text{K}^{-1}$.

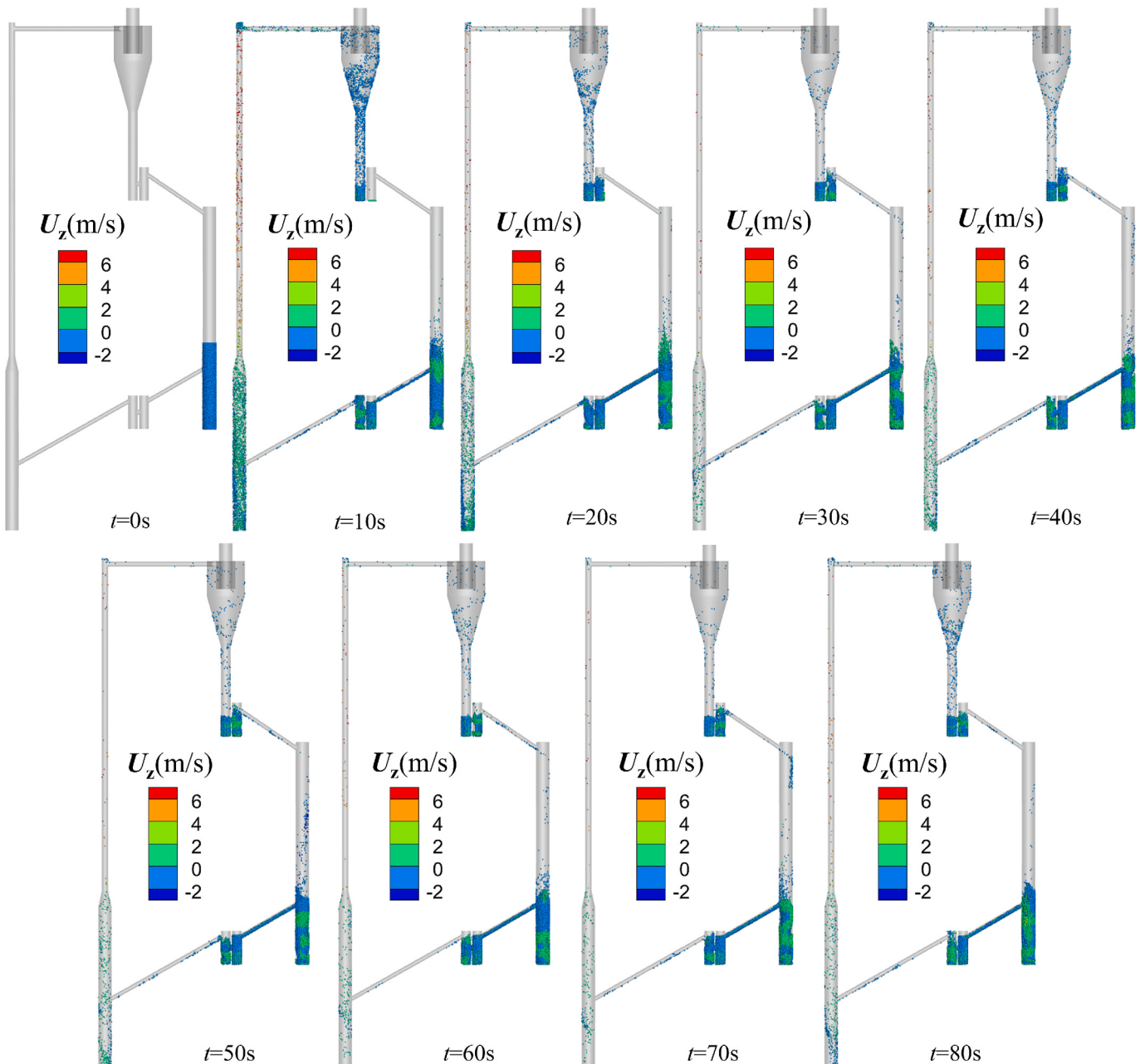


Fig. 3. The variation of particle velocity over time colored by axial particle velocity (U_z , m/s) in the CFB.

When there is any spatial difference in the temperature distribution of the particles, the heat transfer between the particles changes. The formula is as follows [30,31]:

$$\theta_p \rho_p C_p \frac{\partial T_p}{\partial t} = \nabla \cdot (k_{eff} \nabla T_p) \quad (9)$$

C_p is particle specific heat, $\text{kJ} \cdot \text{kg}^{-1} \cdot \text{K}^{-1}$. T_p is particle temperature, K. k_{eff} is the particle effective thermal conductivity, $\text{W} \cdot \text{m}^{-1} \cdot \text{K}^{-1}$, limited to the range [0,1]. The effective thermal conductivity depends on the particle volume fraction by the following relation [30,31]:

$$k_{eff} = k_p \frac{3\theta_p - 1}{2} \quad (10)$$

where k_p represents the mass-weighted average of thermal conductivities of particle materials, $\text{W} \cdot \text{m}^{-1} \cdot \text{K}^{-1}$. The radiation between a thermal wall cell and particles, q_{wp} , is calculated as [30,31]:

$$q_{wp} = A_w F_{wp} \alpha_{wp} \sigma (T_w^4 - T_p^4) \quad (11)$$

where A_w is the area of the thermal wall, m^2 . T_w is the temperature of the wall, K. T_p is the mass-weighted average temperature of particles in a cell, K. F_{wp} is a calculated view factor. σ is the Stefan-Boltzmann constant. α_{wp} is the effective emissivity between the wall and the particles in a cell.

$$\alpha_{wp} = \left(\frac{1}{\alpha_p} + \frac{1}{\alpha_w} - 1 \right)^{-1} \quad (12)$$

where α_p is the volume-weighted average of particle emissivity, α_w is the specified emissivity of the wall.

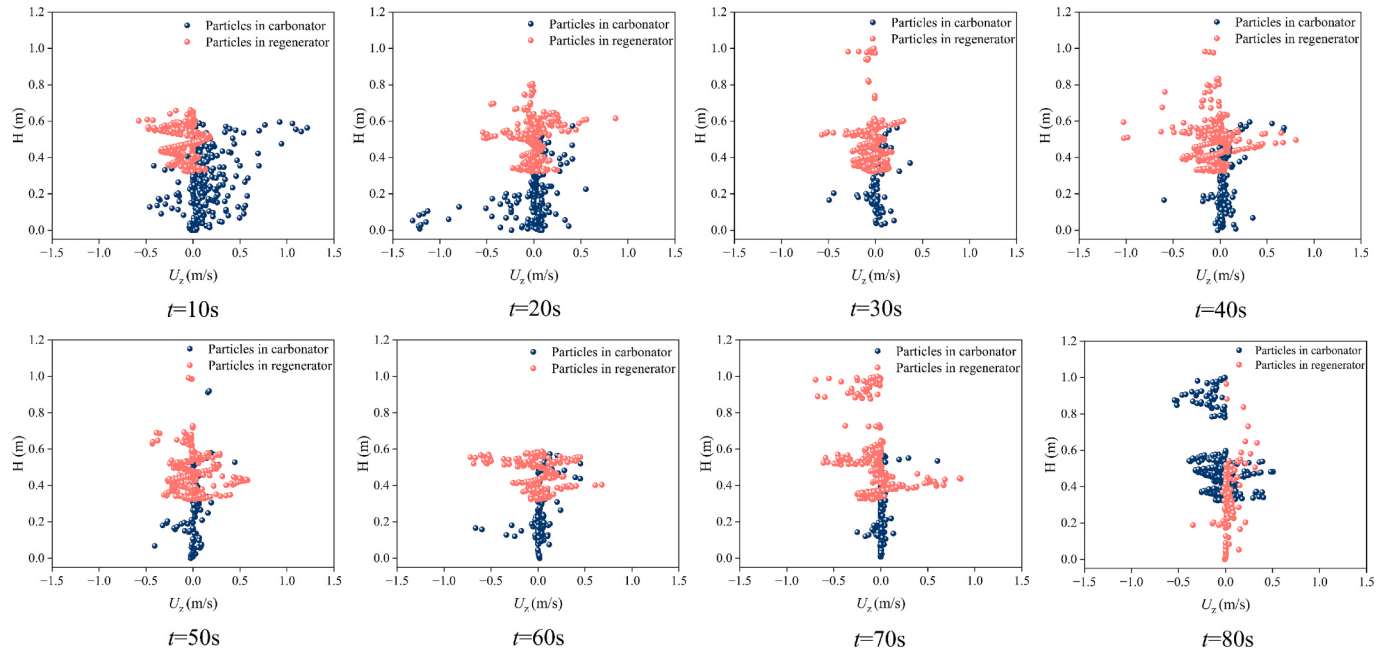


Fig. 4. Detailed distribution of instantaneous axial particle velocities in the CFB.

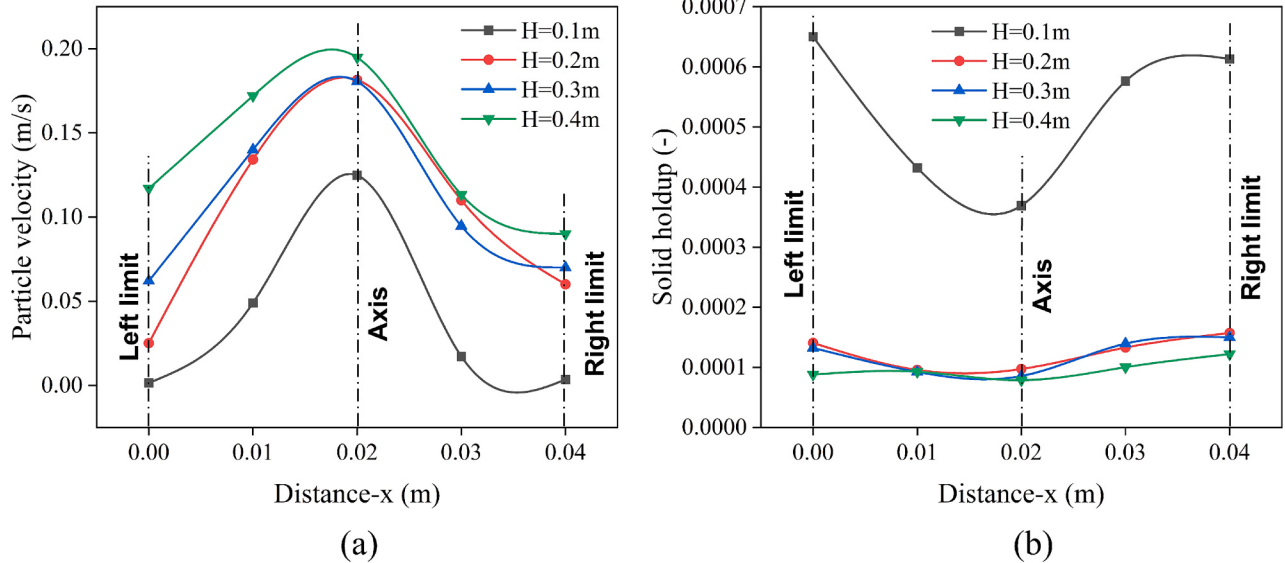


Fig. 5. Time-averaged radial distribution of carbonator at different heights: (a) Particle velocity; (b) Solid holdup.

2.2. Inter-phase drag model

In this study, there are both particle-dense regions and particle-lean regions, so the Gidaspow drag force model [32], which is more universal for a wider particle density range, is used to present the drag force between gases and particles. The Gidaspow drag model uses the Wen and Yu correlation for dilute particle loadings and the Ergun relationship for dense particle loadings, and the corresponding equations are as follows [33]:

$$F(\phi, Re) = \begin{cases} F_{WY} & \phi \leq 0.2 \\ F_E & \phi > 0.2 \end{cases} \quad (13)$$

$F(\phi, Re)$ is the drag model function used as a multiplier to Stokes drag; the variable ϕ represents the combined volume fraction of particles and bubbles. The Wen-Yu model is based on single particle drag models

plus a dependence on the fluid volume fraction θ_f to account for the particle packing, as reflected in Eqs. (14) and (15). The Ergun drag model was developed from dense bed data and is therefore only valid for those systems, as reflected in Eq. (16).

$$F_{sp} = \begin{cases} 1 + 0.15Re^{0.687} & Re \leq 1000 \\ 0.44 \frac{Re}{24} & Re > 1000 \end{cases} \quad (14)$$

$$F_{Wen-Yu}(\phi, Re) = F_{sp}\theta_f^{-3.65} \quad (15)$$

$$F_{Ergun}(\phi, Re) = \frac{c_0 Re + c_1(1 - \theta_f)}{18\theta_f^2} \quad (16)$$

In Eq. (16), $c_0 = 2$ is the non-linear coefficient, $c_1 = 180$ is the linear coefficient.

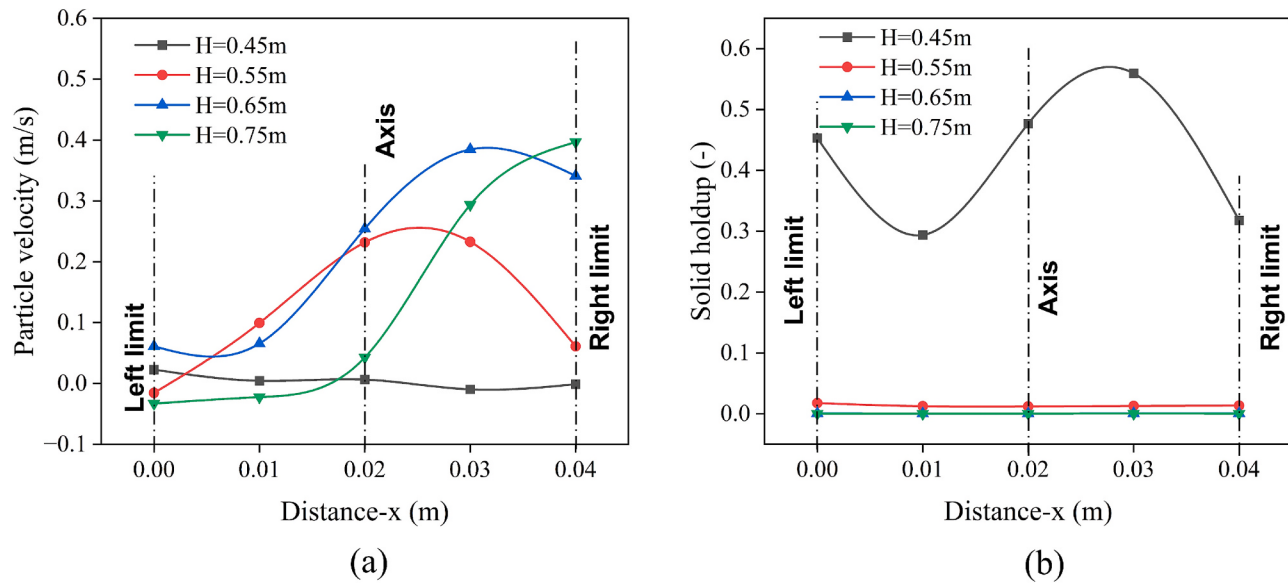


Fig. 6. Time-averaged radial distribution of regenerator at different heights: (a) Particle velocity; (b) Solid holdup.

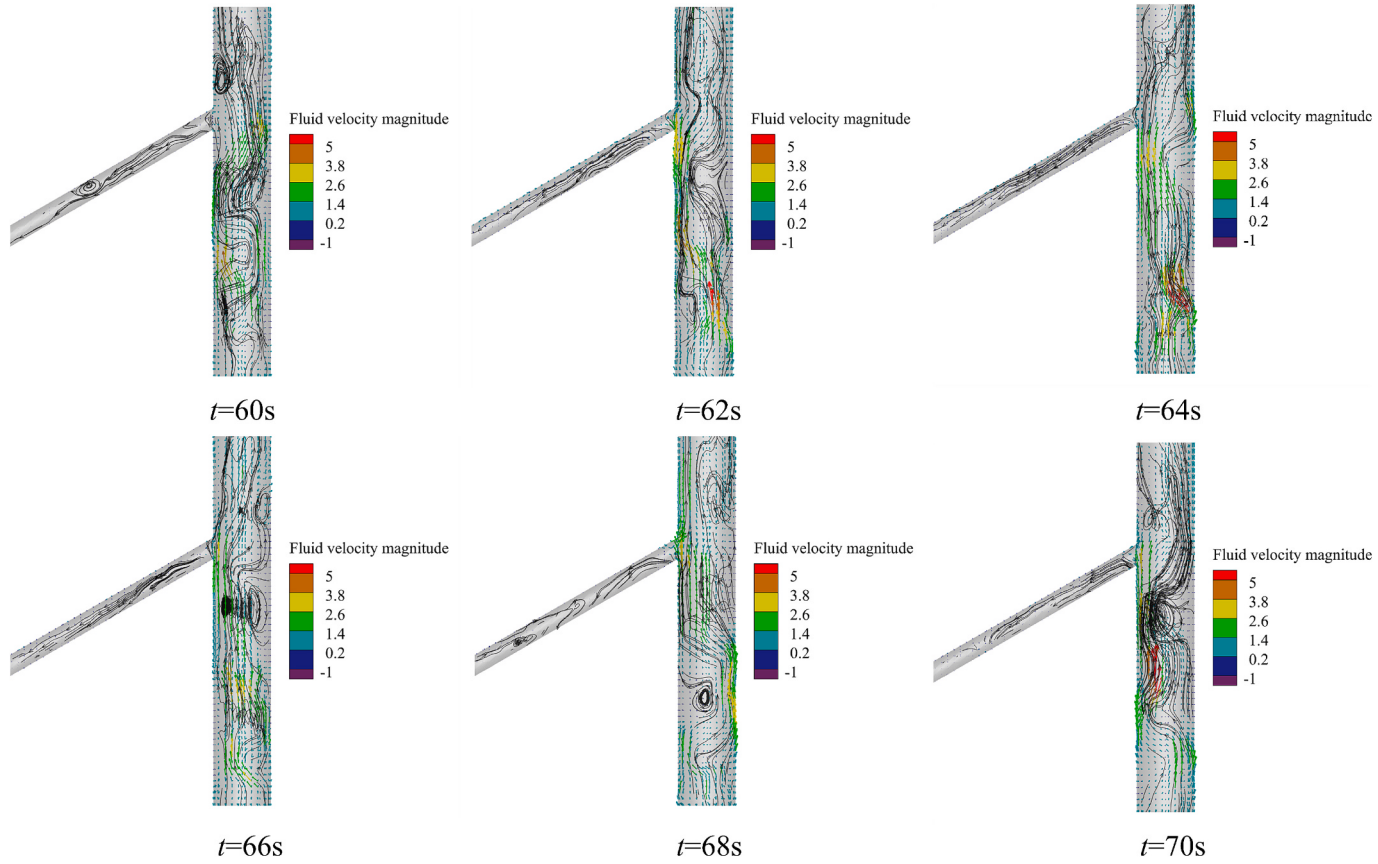


Fig. 7. Local configuration of instantaneous fluid velocity vectors and streamlines for the downflow seal valve and regenerator.

2.3. Simulation settings

The present study utilizes a three-dimensional laboratory-scale circulating fluidized bed (CFB) system, with its complete geometry depicted in Fig. 1(a). The corresponding boundary condition configuration is presented in Fig. 1(b), while Fig. 1(c) and (d) display the computational grid schematics.

The circulating fluidized bed comprises a carbonator, a regenerator,

a cyclone separator, an upper loop seal (ULS), and a lower loop seal (LLS). The carbonator is positioned on the left side, and the regenerator is on the right. The carbonator has a total height of 500 mm and is connected to the riser through a 50 mm high connector. The riser itself measures 1040 mm in height, while the regenerator stands at 700 mm. Gas is introduced from the bottom of both reactors and the flow sealing valves. In this study, calcium oxide (CaO) served as both the fluidized particle and the initial bed material. It was stacked at the bottom of the

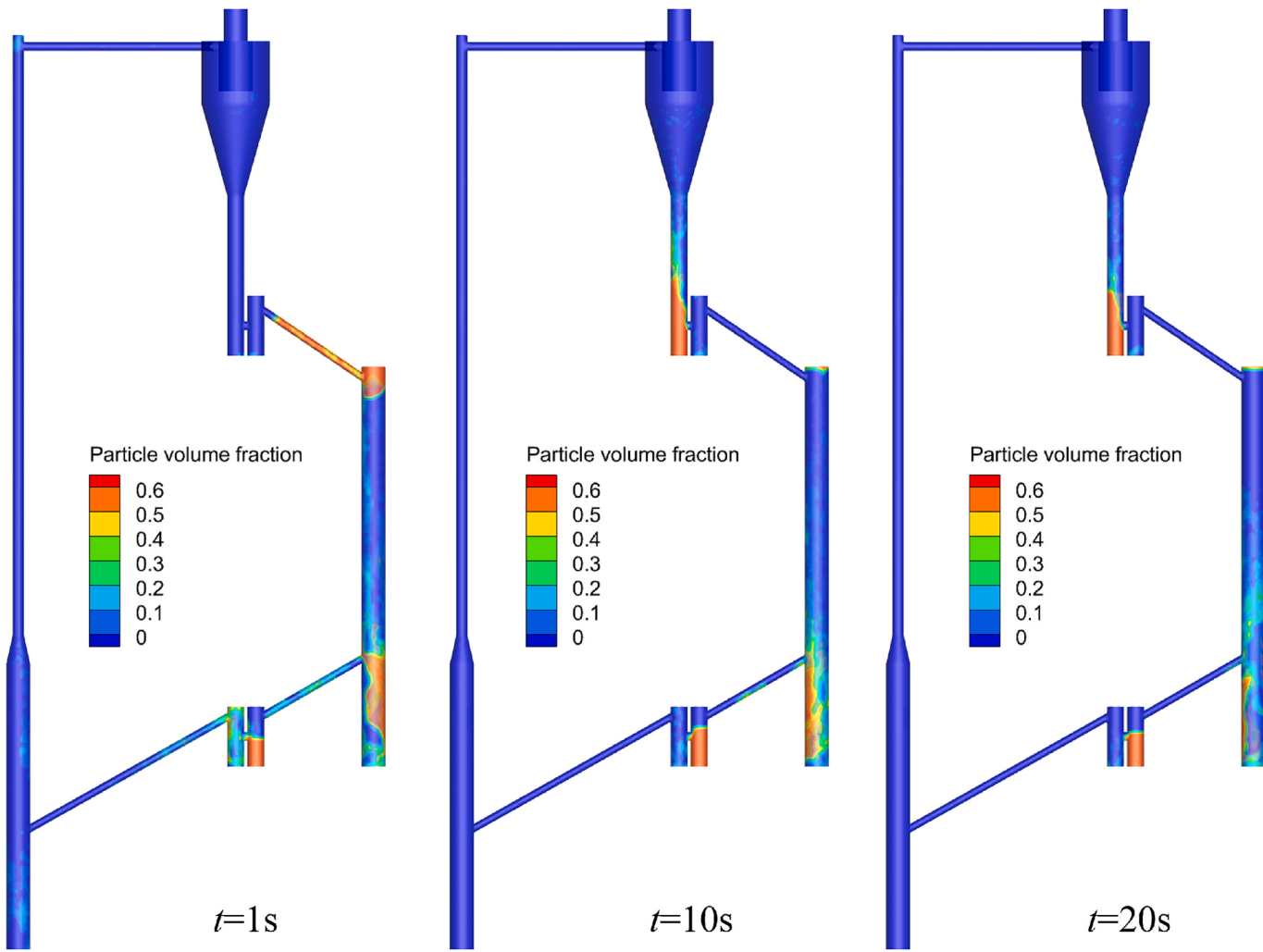


Fig. 8. The instantaneous particle volume fraction in the reactor in thermal state with the same inlet rate as the cold state.

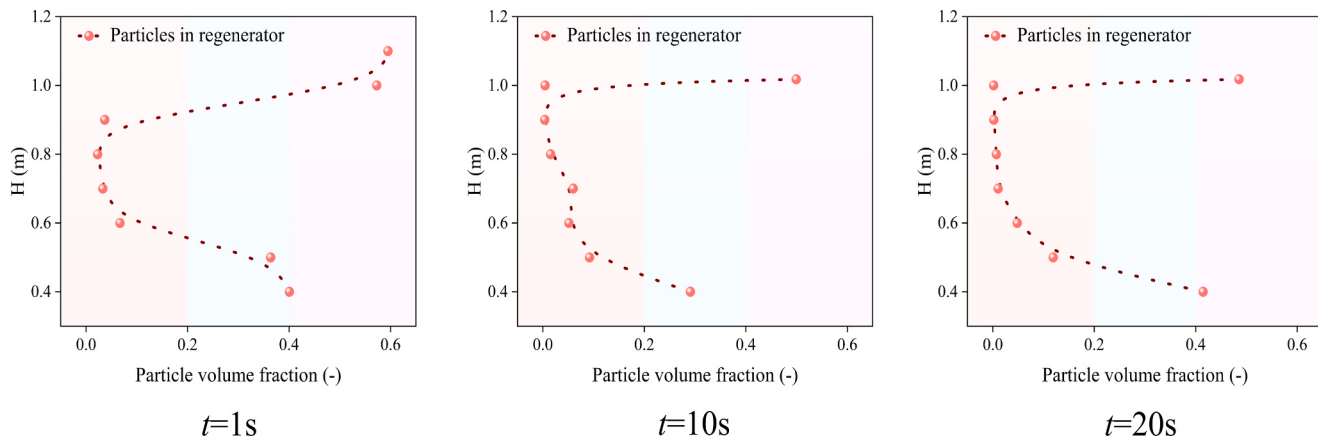


Fig. 9. Instantaneous cross-sectional mean volume fraction at different heights in the regenerator.

regenerator, with a density of 3350 kg/m^3 and a uniform particle size of $150 \mu\text{m}$. Pressure measurement points were distributed throughout the system with the following configuration: P1 at the carbonator base, P2 at 110 mm below the riser top, P3 at 100 mm below the regenerator top, and P4 at the regenerator bottom. The reactor inlets and flow sealing valves were defined as velocity inlets, while the cyclone separator outlet and regenerator outlet were specified as pressure outlets. Monitoring

planes were strategically established in both reactors to track particle flows. For the carbonator, the monitoring plane encompassed the particle inlet (down-flow sealing valve–carbonator junction) and the outlet. Similarly, the regenerator's monitoring plane included the particle inlet (up-flow sealing valve–regenerator connection) and the outlet (down-flow sealing valve–regenerator interface). The simulation was conducted for a total duration of 80 s, with an average start-up time of 60 s. Key

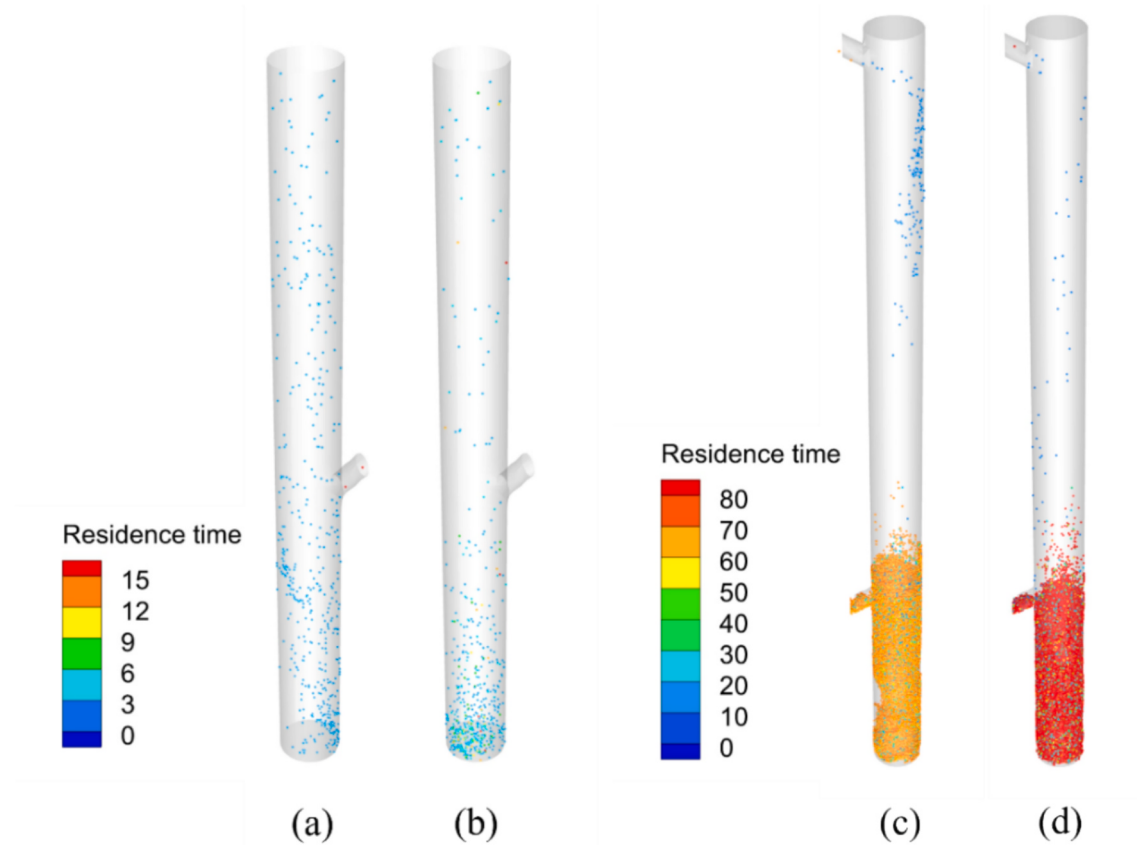


Fig. 10. Particle residence time distribution. (a) Cold state in carbonator; (b) Thermal state in carbonator; (c) Cold state in regenerator; (d) Thermal state in regenerator.

simulation parameters are presented in Table 1.

3. Results and discussion

3.1. Mesh independence analysis and model validation

To verify grid independence, three different grid domains were tested: 31,000 (coarse grid), 53,000 (medium grid), and 71,500 (fine grid). The variations in pressure drop across the carbonator were examined for different grid sizes. As shown in Fig. 2(a), after 30 s of fluidization, the pressure-drop curves for the 53,000 and 71,500 grid counts gradually converged. Additionally, an analysis of fluid velocity at the outlet of the cyclone separator was conducted, as illustrated in Fig. 2(b). When the grid count exceeded 53,000, the fluid velocity stabilized and fluctuated around a fixed value. Therefore, to balance computational time and accuracy, the medium grid was ultimately selected as the grid size for the calculations.

To validate the gas–solid two-phase flow model, the model data were compared with experimental data. Fig. 2(c) and (d) illustrate the pressure drop variations when the inlet air flow rate to the carbonator is 3.2×10^{-3} kg/s and the regenerator is 4.5×10^{-4} kg/s, respectively. Simulation results indicate that the pressure drops of the carbonator and the regenerator fluctuate around 0.75 kPa and 4 kPa, respectively, aligning well with the experimental results and showing good consistency. Therefore, the established model can accurately predict the gas–solid flow processes occurring in the circulating fluidized bed.

3.2. General flow patterns

Fig. 3 illustrates the temporal evolution of particle velocity in a circulating fluidized bed with axial velocity (U_z) color mapping. The

particle circulation follows a well-defined cyclic pathway through the dual-reactor system. The system initiates with particle accumulation in the regenerator. Upon introduction of fluidizing gas, particles are conveyed through the downflow loop seal into the carbonator. The resulting gas–solid mixture subsequently flows into the cyclone separator, where efficient particle separation occurs before their return to the regenerator, establishing a continuous circulation cycle. The carbonator operates as a transporting fluidized bed, while the regenerator functions as a slowly bubbling fluidized bed. The gas–solid flow pattern reached a dynamic steady state after 30 s. It is evident that particles exhibited a high axial velocity in the riser above the carbonator. In both the carbonator and regenerator, the velocity distribution of the particles at different heights varied, which was a result of the particle–particle interactions and particle–wall interactions. Once fluidization has stabilized, the particle velocities exhibit a characteristic pattern of low velocity near the walls and higher velocity in the middle zone. Fig. 4 statistically presents the temporal evolution of particle axial velocity distributions in both reactors. During the initial 30-second transient period, the carbonator exhibits particularly wider velocity dispersion than observed in the regenerator. Following system stabilization ($t > 30$ s), the velocity distributions converge to a stable range of -0.5 to 0.5 m/s for most particles.

Figs. 5 and 6 present time-averaged velocity distributions and radial distributions of solids concentration at different heights in the carbonator and regenerator, respectively. In the carbonator, a clear symmetrical distribution curve is observed, with low velocities in the near-wall region and high velocities in the central region, indicating the presence of a “core-annulus profile” [34]. Moreover, with increasing height, the particle velocities gradually increased. The radial distribution of solid concentration showed an opposite trend to the velocity profile, where the solid concentration was higher in the near-wall region compared to

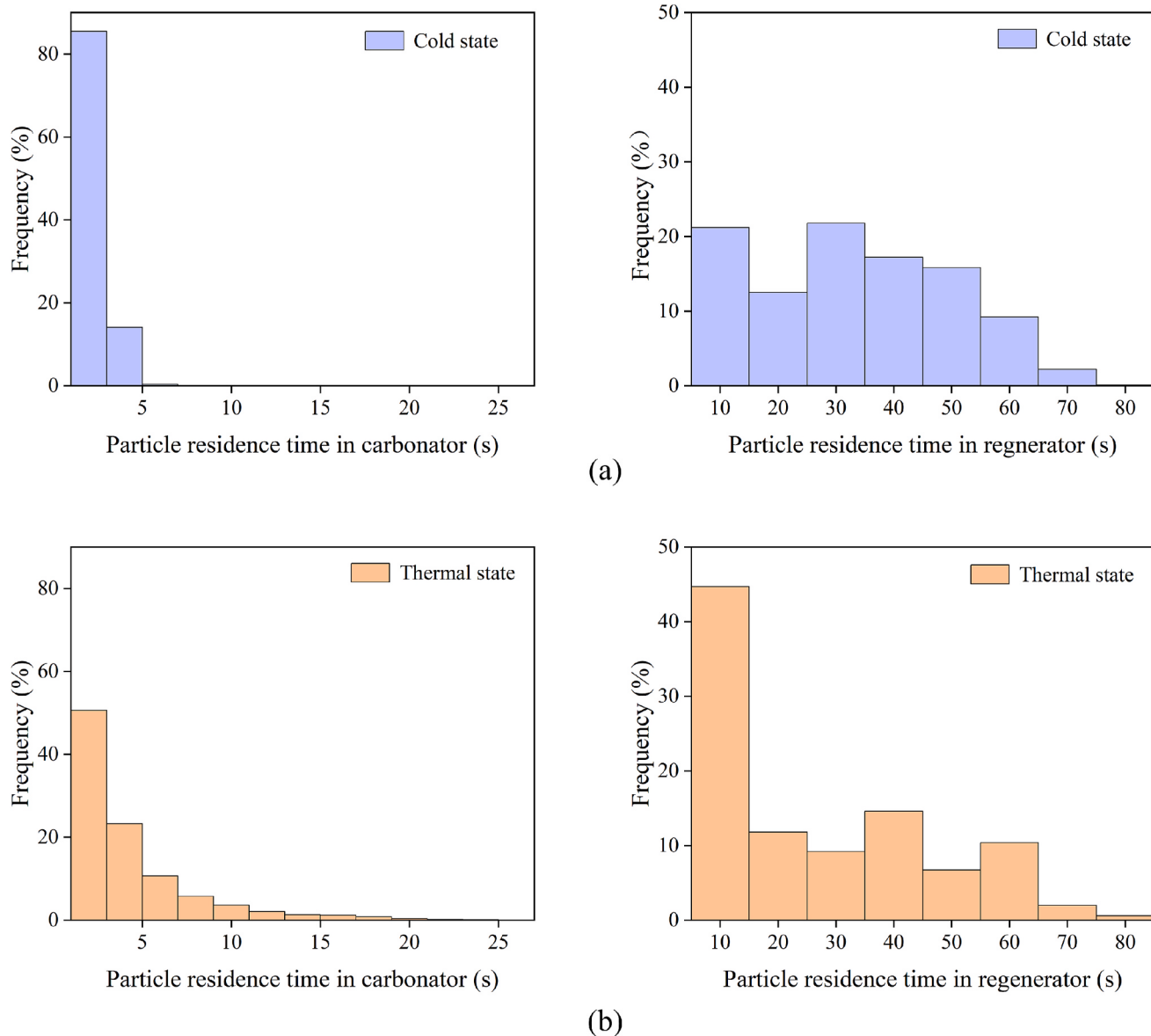


Fig. 11. Statistical frequency histogram of particle residence time in the carbonator and regenerator: (a) Cold state; (b) Thermal state.

the central region. At $H = 0.1$ m, the difference in solid concentration between the wall and the central region was considerable; as the height increased, the solid concentration became more uniformly distributed radially, and the solid holdup curve flattened. In the regenerator, the particles returning from the cyclone separator collided and mixed with the upward-moving particles within the reactor. The intensive gas–solid exchange that transpired between the particles and the downflow loop seal engendered a more complex set of phenomena in the regenerator. In this instance, the axial velocity of particles manifested an irregular radial distribution. As illustrated in Fig. 6(a), the flow velocities are lower in the leftmost region (bounded by $x = 0$). Consequently, this region exhibits a relatively higher solids concentration, as evidenced in Fig. 6(b). At $x = 0.03$ m, the particle velocity exhibited a slight increase, concurrent with a decrease in solid concentration. Overall velocities on the left side were found to be lower in comparison to those on the right. Fig. 7 shows a localized plot of the transient velocity vectors and streamlines of the fluid in the downflow seal valve and the regenerator over a period of 60–70 s. It is evident that a portion of the gas up-flow in the regenerator was split to the left side tube, thereby reducing the up-flow velocity and, consequently, the particle velocity on the left side

[12,35].

3.3. Particle residence time

A thorough understanding of particle RTD in circulating fluidized beds is crucial for the design and optimization of fluidization processes.

Upon entering the monitoring plane, the particles' movement is tracked by an iterator that calculates their residence time [31]. The residence time is then updated in accordance with the time step, thereby providing a comprehensive measurement of the particles' total residence time within the reactor.

This study analyzed the residence time of particles under both thermal and cold conditions. Fig. 8 shows the distribution of particles in the reactor when the parameters of the thermal state are the same as those of the cold state. At $t = 1$ s, a significant proportion of particles were observed to accumulate above the regenerator. This phenomenon can be attributed to the magnified velocity resulting from the expansion of gases in a thermal state. Following 10 and 20 s of fluidization, the number of particles accumulating above the regenerator decreased; however, some particles still gathered at the outlet of the regenerator. As

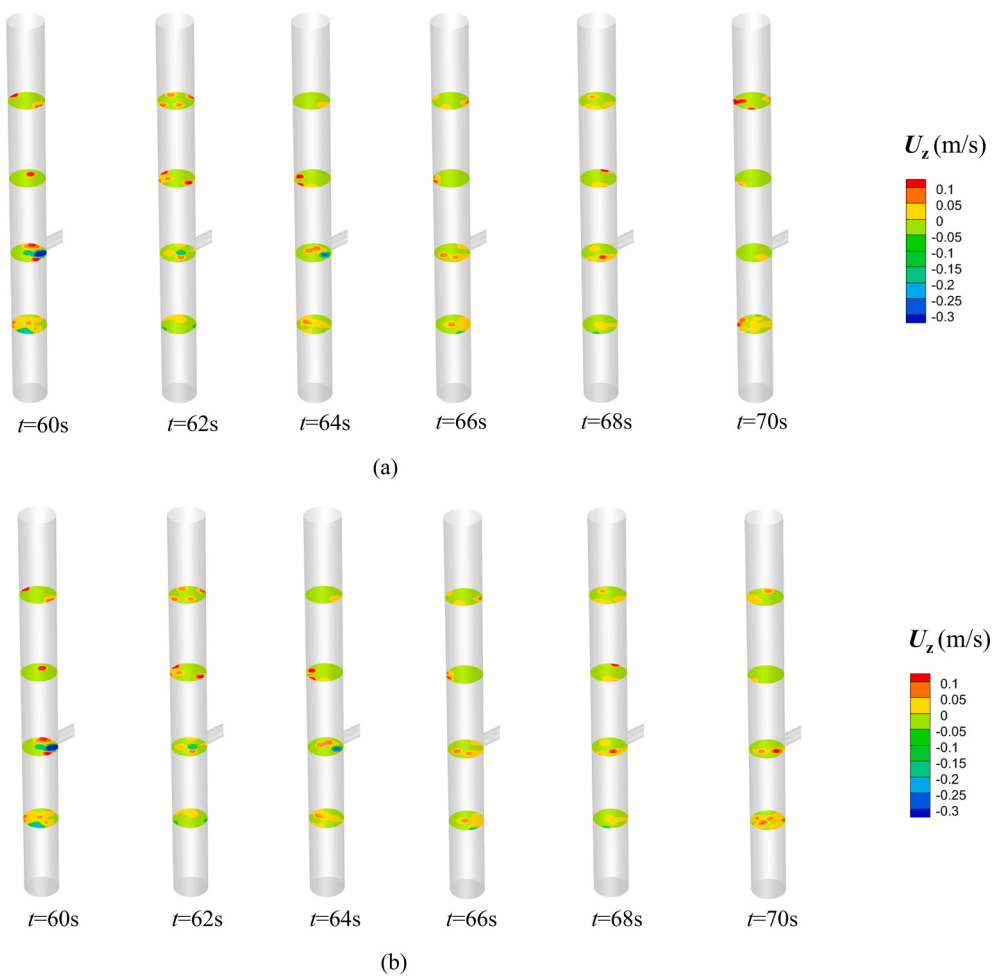


Fig. 12. Instantaneous velocity distribution of particle cross-section in the carbonator. (a) Cold state; (b) Thermal state.

demonstrated in Fig. 9, this phenomenon is more readily apparent when viewed visually. In this study, the regenerator functions as a bubbling fluidized bed, with the gas velocity through the solid particle bed ranging from the minimum fluidization velocity (u_{mf}) to the turbulent transportation velocity (u_{tr}). Consequently, the regenerator transitioned from the originally bubbling fluidization to the transportation state. Therefore, it can be concluded that the simulation parameters suitable for cold-state conditions do not apply to thermal-state scenarios, necessitating a readjustment of the inlet air flow rate.

Fig. 10 illustrates the phenomenon of uneven distribution of particle residence time in the two reactors. Blue particles have a shorter residence time and can pass directly through the carbonator and regenerator, while red particles have a longer residence time. It has been found that particles in the carbonator usually have a shorter residence time than those in the regenerator. Furthermore, even at the same height, the residence time of the particles varies. Lower heights show more colors, suggesting that they may have undergone back-mixing within the reactor.

Once the system reached a stable flow, a flow time of 60–80 s was selected for statistical analysis of the particle residence time within this range. The results are shown in Fig. 11 and indicate that, in both the cold and thermal states, the particle RTD profile exhibits an “early peak and a long tail”. Those particles with very long residence time must undergo upward and downward movement (shown in Supplementary video), thus present in the reactor for so long. This further confirms the presence of the back-mixing phenomenon.

3.4. Solids back-mixing characteristics

The back-mixing phenomenon of particles depends on their flow behavior inside the reactor. Fig. 12 and Fig. 13 illustrate the cross-sectional velocity distributions of particles in the cold and thermal states within the carbonator and regenerator, respectively. Analysis of the cross-sectional velocity of particles shows significant downward movement behavior at the bottom of the reactor in both cold and thermal states. Additionally, the particles exhibit more pronounced downward movement behavior in the regenerator than in the carbonator, which is against the general movement caused by the gas drag. This behavior results in particles having a long residence time inside the reactor, which is typically the cause of back-mixing phenomena. As the height increases, fewer particles move downwards, and the degree of back-mixing decreases.

3.5. Particle temperature distribution and evolution

In the calcium looping process, the carbonator is generally around 923 K, and the decarbonation reaction for the regenerator is around 1173 K. The range of particle temperatures can be modified by radiation between the thermal wall and nearby particles, particle-to-particle heat conduction, and particle-gas heat transfer. The temperature distribution of the particles under thermal conditions varies over time, as demonstrated in Fig. 14. Initially, all particles were loaded in the regenerator at 1173 K. As the fluidization and circulation processes unfolded, a discernible variation in temperature was observed among the particles within the two reactors. Once the particle circulation reaches a steady

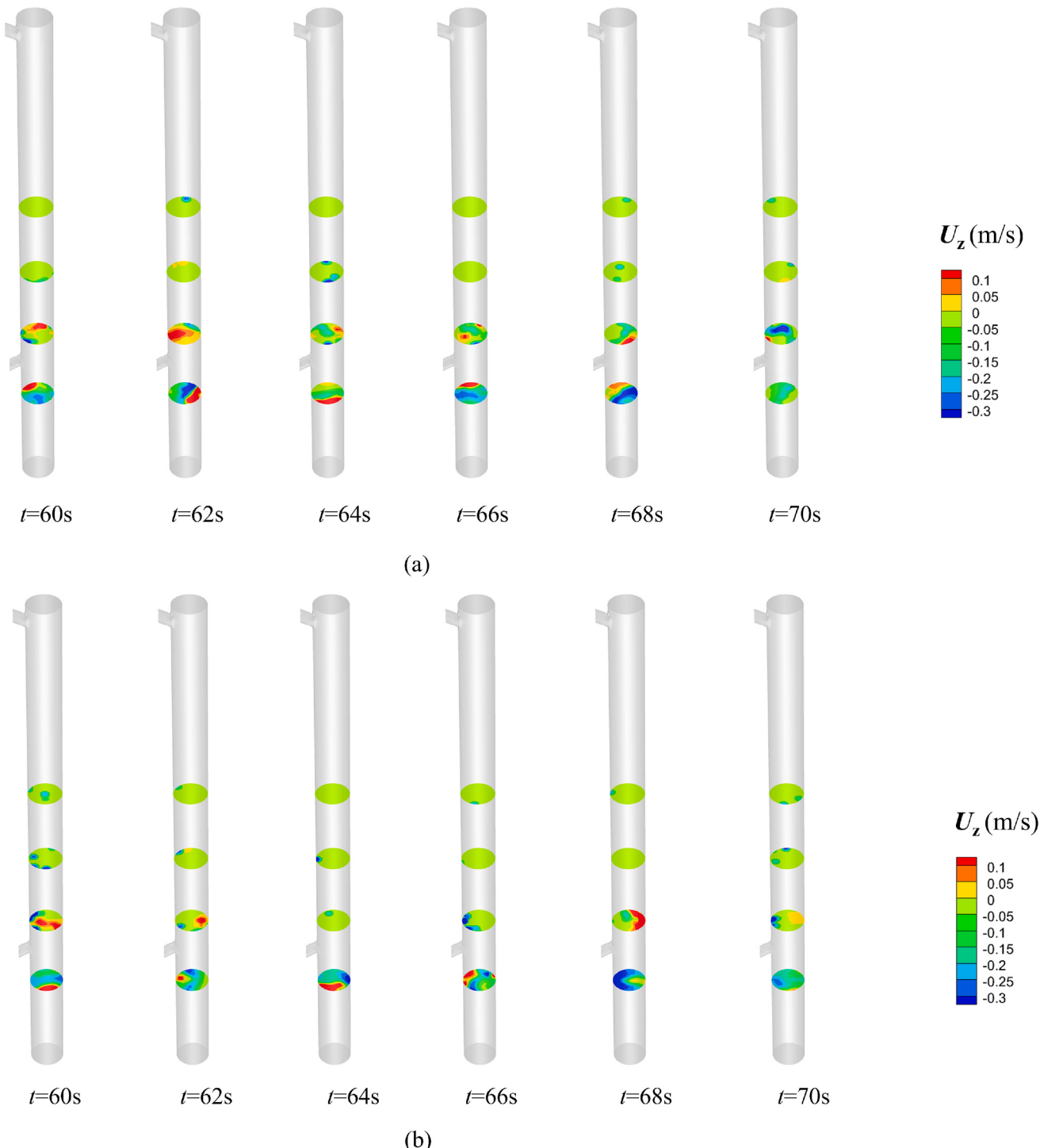


Fig. 13. Instantaneous velocity distribution of particle cross-section in the regenerator. (a) Cold state; (b) Thermal state.

state, the temperature distribution stabilizes. As shown in Fig. 15, the lowest recorded temperature was consistently observed at the base of the carbonator, attributable to the low temperature of the fluidizing gas. The maximum temperature was observed in the regenerator as expected.

The outlet temperatures of the particles from both the carbonator and the regenerator were recorded over a duration of 60 to 80 s when the circulation was steady. Fig. 16(a) illustrates the time-averaged temperature distribution of the particles at the outlet of the carbonator, which ranged between 700 and 800 K, indicating a significant temperature difference from the reactor wall. This is due to the fact that a majority (>70 %) of particles in the carbonator experienced notably

short residence periods (0–5 s), according to the RTD profile shown in Fig. 11(a). Such short contact times substantially decrease heat transfer efficiency at the particle–wall interface. Another contributing factor is the excessively high gas velocity at the carbonator inlet, which cools the particles at the bottom of the carbonator. Additionally, from Fig. 14, upon achieving steady-state fluidization conditions (at $t = 50$ s), a pronounced temperature differential emerges between the particle in the left and right sides of the loop seal chamber. This discrepancy arose from the continuous introduction of room temperature gas on the left side of the loop seal, further causing a significant temperature difference between the particle and the reactor wall.

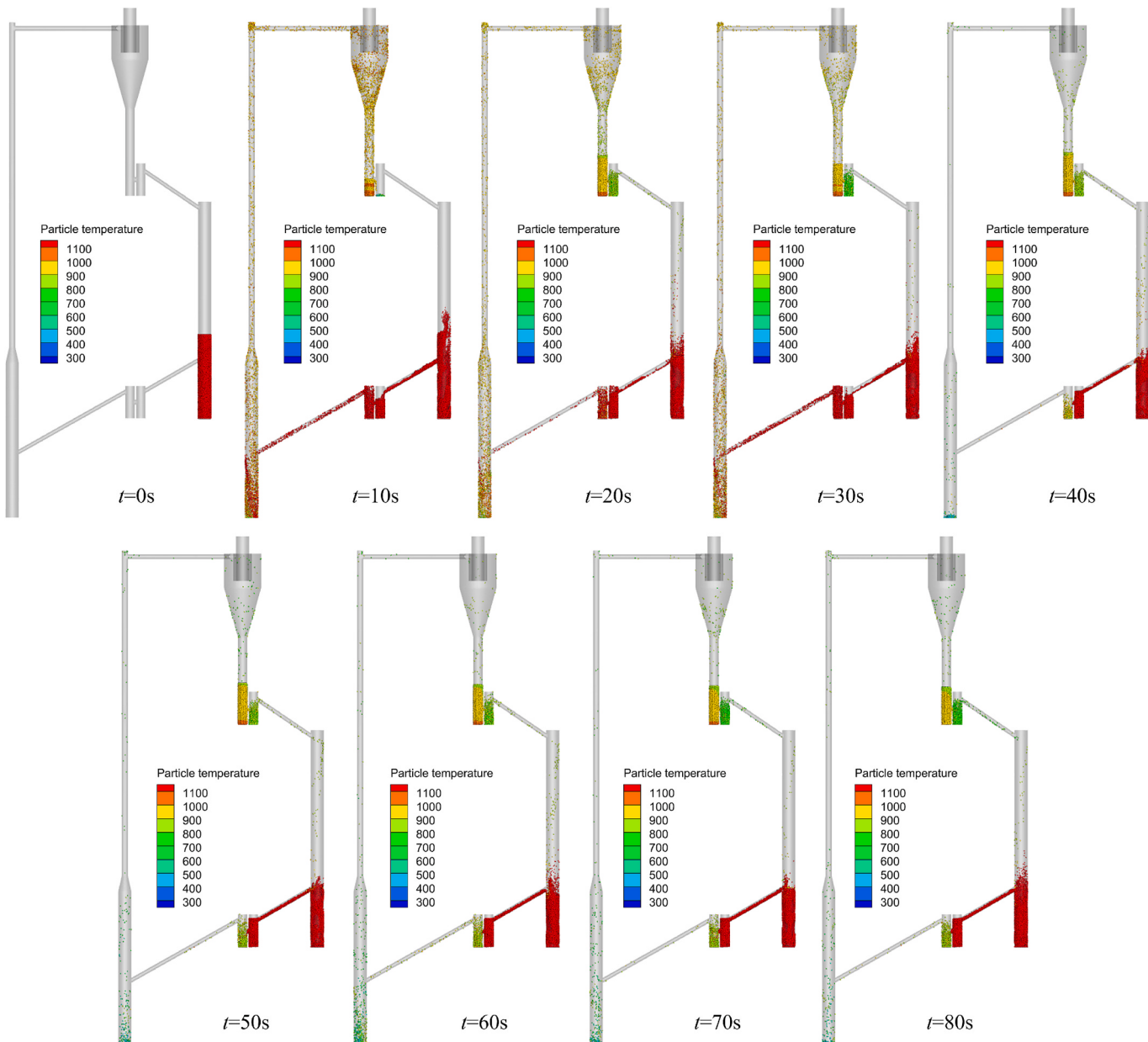


Fig. 14. Time evolution of particle temperature distribution in thermal state.

Fig. 16(b) displays the time-averaged temperature of the particles at the outlet of the regenerator, which ranges from 1140 to 1160 K, demonstrating a marginal temperature difference from the regenerator's wall. As evidenced by the RTD profile in **Fig. 11(b)**, particles in the regenerator exhibit substantially longer residence times than those in the carbonator. This extended duration facilitates enhanced thermal exchange with the reactor walls, thereby improving overall heat transfer efficiency.

4. Conclusion

Based on the MP-PIC method, a three-dimensional, lab-scale CFD model was established for the flow process of calcium looping to investigate the gas–solid fluid dynamics in a circulating fluidized bed. Analyses were conducted on the particle RTD and solid back-mixing behavior under both cold and thermal conditions, aiming to explore the main factors causing solid back-mixing. The carbonator exhibited a standard “core-annulus structure” in its axial velocity and particle

distribution under stable conditions. In contrast, the regenerator showed an irregular distribution. This is attributed to the collisions among the upward-moving particles and those circulating back from the loop seal, resulting in a more complex gas–solid flow pattern inside the reactor. During the thermal-state simulation of the CFB, when the parameters were set to be consistent with those in the cold state, a significant accumulation of particles was observed at the regenerator outlet. This is due to the continuous increase in gas temperature in the thermal state, which changed both the density and viscosity of the gas, leading to excessively high gas velocity. This behavior does not conform to the bubbling fluidized bed flow pattern expected in this CFB. Therefore, the simulation parameters used in the cold state are not applicable to the thermal-state simulations. Under both cold and thermal states, the particle residence time in both the carbonator and regenerator exhibited uneven distributions, with certain particles evidently having longer residence times. Additionally, the particle RTD profile shows characteristics of “early peaks and long tails,” confirming the presence of back-mixing phenomena within the CFB. Compared to the carbonator, back-

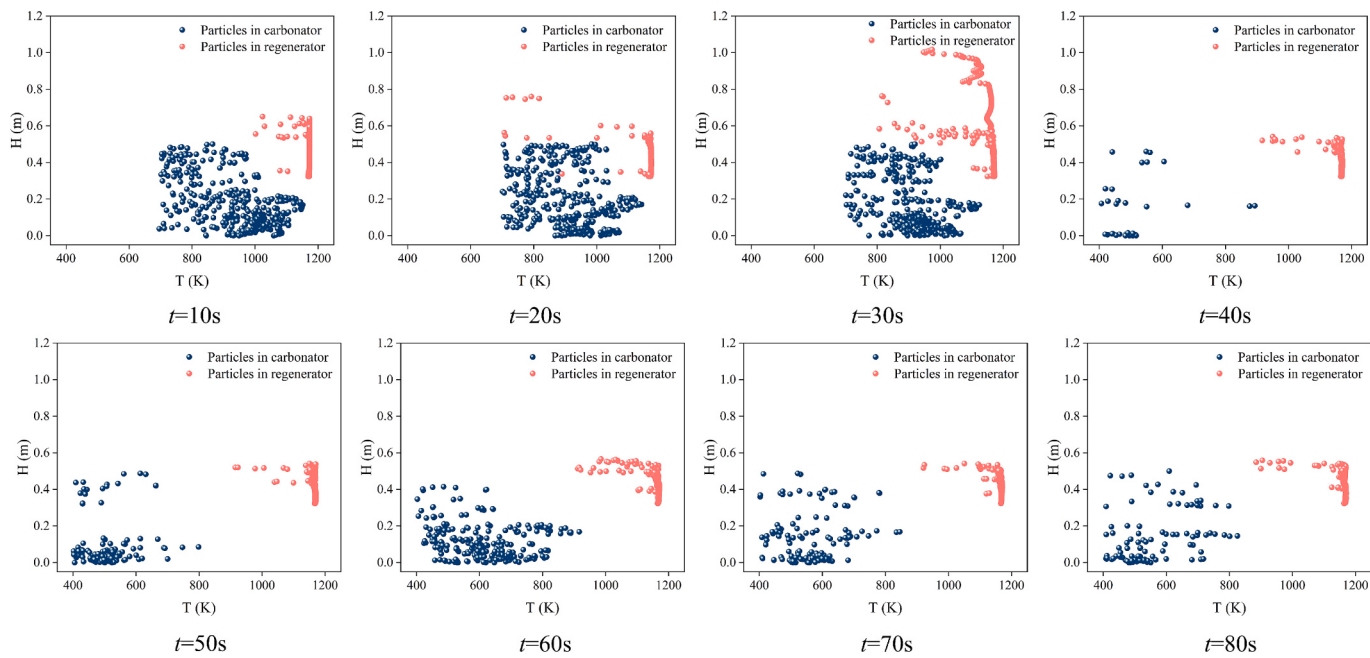


Fig. 15. Detailed distribution of instantaneous axial particle temperatures in the CFB.

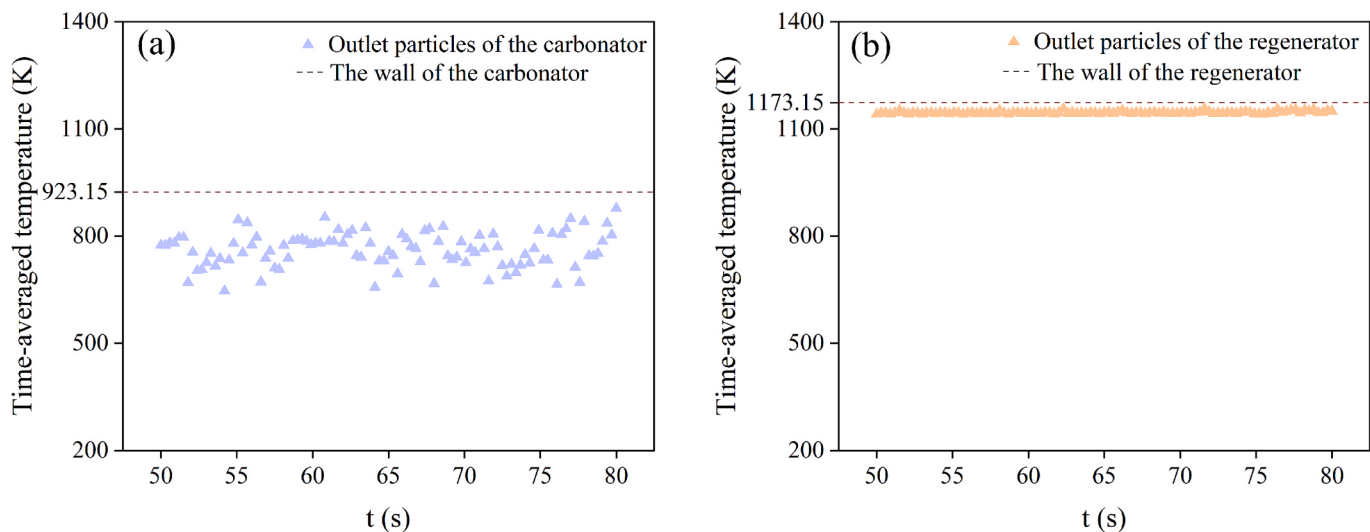


Fig. 16. Time-averaged temperature of outlet particles in the (a) Carbonator; (b) Regenerator.

mixing is more severe in the regenerator, and the degree of back-mixing gradually diminishes with increasing height. An analysis of the axial velocities of particles at different cross-sections of the reactor revealed that a significant number of particles move downward in the bottom regions, leading to extended residence times. Residence time had an evident effect on the temperature distribution of particles in the CFB. Particle temperature distribution showed that the particles in the regenerator could reach the desired temperature due to sufficient residence time, but the particles in the carbonator were 100–200 K lower than the set temperature of the reactor wall due to the insufficient residence time. This study provided practical guidance for further optimization of operating conditions and CFB reactor design.

CRediT authorship contribution statement

Junchao Yang: Visualization, Validation, Software, Data curation.
Dongkuan Zhang: Writing – review & editing, Validation.
Li Liu:

Methodology. **Yuanbo Xie:** Resources. **Yingnan Du:** Resources. **Aimin Li:** Funding acquisition. **Changlei Qin:** Validation, Resources, Data curation. **Guozhao Ji:** Writing – review & editing, Writing – original draft, Supervision, Software, Methodology, Investigation, Funding acquisition, Formal analysis, Data curation, Conceptualization.

Declaration of competing interest

The authors declare that they have no known competing financial interests or personal relationships that could have appeared to influence the work reported in this paper.

Acknowledgements

The financial support from the National Key Research and Development Program of China [2025YFE0109700], Fundamental Research Funds for the Central Universities [DUT24ZD103-2023JH2/

101700282], and Liaoning Provincial Science and Technology Plan Project [2023JH1/10400007] are appreciated. The technical support from Dr. Xuefeng Xiang in Hi-Key was also appreciated.

Appendix A. Supplementary data

Supplementary data to this article can be found online at <https://doi.org/10.1016/j.applthermaleng.2025.127937>.

Data availability

Data will be made available on request.

References

- [1] E. Martin-Roberts, V. Scott, S. Flude, G. Johnson, R.S. Haszeldine, S. Gilfillan, Carbon capture and storage at the end of a lost decade, *One Earth* 4 (2021) 1569–1584.
- [2] J. Lin, K. Luo, S. Wang, J. Fan, Multi-scale insights of chemical looping combustion in a three-dimensional bubbling fluidized bed, *Chem. Eng. J.* 474 (2023) 145806.
- [3] G. Cook, P. Zakkour, S. Neades, T. Dixon, CCS under article 6 of the Paris agreement, *Int. J. Greenhouse Gas Control* 134 (2024) 104110.
- [4] S. Chen, J. Liu, Q. Zhang, F. Teng, B.C. McLellan, A critical review on deployment planning and risk analysis of carbon capture, utilization, and storage (CCUS) toward carbon neutrality, *Renew. Sustain. Energy Rev.* 167 (2022) 112537.
- [5] P. Wang, B. Shi, N. Li, R. Kang, Y. Li, G. Wang, L. Yang, CCUS development in China and forecast its contribution to emission reduction, *Sci. Rep.* 13 (2023) 17811.
- [6] J. Lin, K. Luo, S. Wang, J. Fan, Numerical simulation of gasifier optimization for combined hydrogen production and carbon reduction in a chemical looping gasification (CLG) system, *Chem. Eng. Sci.* 301 (2025) 120694.
- [7] A.S. Bhowm, B.C. Freeman, Analysis and status of post-combustion carbon dioxide capture technologies, *Environ. Sci. Technol.* 45 (2011) 8624–8632.
- [8] D. Zhou, Y. Wang, Z. Zhang, Y. Zhang, A. Li, J. Luan, G. Ji, Vacuum assisted desorption of sodium zirconate sorbent for enhancing cyclic stability in pre-combustion CO₂ capture, *Carbon Capture Sci. Technol.* 13 (2024) 100277.
- [9] D. Zhou, Y. Wang, M.Z. Memon, W. Fu, Z. Wu, S. Sheng, H. Zhang, G. Ji, The effect of Na₂ZrO₃ synthesis method on the CO₂ sorption kinetics at high temperature, *Carbon Capture Sci. Technol.* 3 (2022) 100050.
- [10] F. Sattari, M. Tahmasebpoor, J.M. Valverde, C. Ortiz, M. Mohammadpourfard, Modelling of a fluidized bed carbonator reactor for post-combustion CO₂ capture considering bed hydrodynamics and sorbent characteristics, *Chem. Eng. J.* 406 (2021) 126762.
- [11] G. Ji, H. Yang, M.Z. Memon, Y. Gao, B. Qu, W. Fu, G. Olguin, M. Zhao, A. Li, Recent advances on kinetics of carbon dioxide capture using solid sorbents at elevated temperatures, *Appl. Energy* 267 (2020) 114874.
- [12] D. Kong, M. Zhou, S. Wang, K. Luo, D. Li, J. Fan, Eulerian-Lagrangian simulation of chemical looping combustion with wide particle size distributions, *Chem. Eng. Sci.* 245 (2021) 116849.
- [13] M. Erans, V. Manovic, E.J. Anthony, Calcium looping sorbents for CO₂ capture, *Appl. Energy* 180 (2016) 722–742.
- [14] Y. Wang, M.Z. Memon, Q. Xie, Y. Gao, A. Li, W. Fu, Z. Wu, Y. Dong, G. Ji, Study on CO₂ sorption performance and sorption kinetics of Ce- and Zr-doped CaO-based sorbents, *Carbon Capture Sci. Technol.* 2 (2022) 100033.
- [15] Y. Song, G. Ji, X. Zhao, X. He, X. Cui, M. Zhao, Effects of drying methods on wet chemistry synthesis of Al-stabilized CaO sorbents for cyclic CO₂ capture, *Energy Fuel* 31 (2017) 12521–12529.
- [16] M. Guo, J. Yu, S. Wang, K. Luo, J. Fan, Study of biomass gasification combined with CO₂ absorption in a dual fluidized bed (DFB) using the Eulerian-Lagrangian method, *Chem. Eng. J.* 483 (2024) 148723.
- [17] A. Coppola, F. Scala, P. Salatino, F. Montagnaro, Fluidized bed calcium looping cycles for CO₂ capture under oxy-firing calcination conditions: Part 1. Assessment of six limestones, *Chem. Eng. J.* 231 (2013) 537–543.
- [18] N. Gao, M. Sliz, C. Quan, A. Bieniek, A. Magdziarz, Biomass CO₂ gasification with CaO looping for syngas production in a fixed-bed reactor, *Renew. Energy* 167 (2021) 652–661.
- [19] A. Stroh, A. Daikeler, M. Nikku, J. May, F. Alabaid, M. von Bohnstein, J. Ströhle, B. Epple, Coarse grain 3D CFD-DEM simulation and validation with capacitance probe measurements in a circulating fluidized bed, *Chem. Eng. Sci.* 196 (2019) 37–53.
- [20] G. Ji, G. Wang, K. Hooman, S. Bhatia, J.C. Diniz da Costa, Simulation of binary gas separation through multi-tube molecular sieving membranes at high temperatures, *Chem. Eng. J.* 218 (2013) 394–404.
- [21] G. Ji, G. Wang, K. Hooman, S. Bhatia, J.C. Diniz da Costa, The fluid dynamic effect on the driving force for a cobalt oxide silica membrane module at high temperatures, *Chem. Eng. Sci.* 111 (2014) 142–152.
- [22] D. Kong, S. Wang, K. Luo, C. Hu, D. Li, J. Fan, Three-dimensional simulation of biomass gasification in a full-loop pilot-scale dual fluidized bed with complex geometric structure, *Renew. Energy* 157 (2020) 466–481.
- [23] M. Zhang, Y. Zhang, D. Ma, A. Li, W. Fu, G. Ji, J. Dong, Numerical investigation on the heat transfer of plastic waste pyrolysis in a rotary furnace, *Chem. Eng. J.* 445 (2022) 136686.
- [24] M. Guo, J. Lin, J. Yu, S. Wang, K. Luo, J. Fan, Configuration optimization of a biomass chemical looping gasification (CLG) system combined with CO₂ absorption, *Renew. Energy* 237 (2024) 121459.
- [25] R.I. Singh, A. Brink, M. Hupa, CFD modeling to study fluidized bed combustion and gasification, *Appl. Therm. Eng.* 52 (2013) 585–614.
- [26] Y. Li, T. Guo, X. Guo, X. Hu, Q. Guo, S. He, Z. Zhou, Computational particle fluid dynamics simulation of gas-solid flow in a 3 MWth dual-circulation fluidized bed for chemical looping process, *Carbon Resour. Convers.* 7 (2024).
- [27] B. Deng, T. Zhou, Y. Zhang, M. Zhang, Z. Huang, H. Yang, Hydrodynamic characteristics in the full-loop circulating fluidized bed under load regulation. Part 2: simulation, *Chem. Eng. Sci.* 264 (2022).
- [28] D.M. Snider, An incompressible three-dimensional multiphase particle-in-cell model for dense particle flows, *J. Comput. Phys.* 170 (2001) 523–549.
- [29] J.C. Bandara, C. Jayarathna, R. Thapa, H.K. Nielsen, B.M.E. Moldestad, M. S. Eikeland, Loop seals in circulating fluidized beds – review and parametric studies using CFD simulation, *Chem. Eng. Sci.* 227 (2020).
- [30] D.S. Smith, A. Alzina, J. Bourret, B. Nait-Ali, F. Pennec, N. Tessier-Doyen, K. Otsu, H. Matsubara, P. Elser, U.T. Gonzenbach, Thermal conductivity of porous materials, *J. Mater. Res.* 28 (2013) 2260–2272.
- [31] D. Gidaspow, Hydrodynamics of fluidization and heat transfer: Supercomputer modeling, *Appl. Mech. Rev.* 39 (1986) 1–23.
- [32] D. Gidaspow, Multiphase flow and fluidization: continuum and Ki, in, Ž.
- [33] R. Beetstra, M.A. van der Hoef, J.A.M. Kuipers, Drag force of intermediate Reynolds number flow past mono- and bidisperse arrays of spheres, *AIChE J.* 53 (2007) 489–501.
- [34] X. Shi, X. Lan, F. Liu, Y. Zhang, J. Gao, Effect of particle size distribution on hydrodynamics and solids back-mixing in CFB risers using CFD simulation, *Powder Technol.* 266 (2014) 135–143.
- [35] S. Chopra, B. Sajjadi, A mechanistic analysis of particle flow in a pulsatile circulating dual fluidized bed for chemical looping technology based on CFD-DEM simulation, *Powder Technol.* 435 (2024) 119260.